INTERNATIONAL JOURNAL FOR NUMERICAL METHODS IN FLUIDS
Int. J. Numer. Meth. Fluids 2004; **46**:767–791
Published online 9 September 2004 in Wiley InterScience (www.interscience.wiley.com). DOI: 10.1002/fld.773

Numerical simulation of heat, mass and momentum transport behaviours in directionally solidifying alloy castings under electromagnetic fields using an extended Direct-SIMPLE scheme

Daming Xu*,†, Yunfeng Bai‡, Jingjie Guo§ and Hengzhi Fu

School of Materials Science and Engineering, Harbin Institute of Technology, Harbin 150001, People's Republic of China

SUMMARY

A Direct-SIMPLE scheme is further extended for numerical simulations of heat and species mass transfer, and liquid flow behaviours in solidification processes of shaped alloy castings under various electromagnetic (EM) fields, based on a binary continuum model (a solidification transport phenomena/processes (STP)-based dendrite solidification model). Unlike in a SIMPLE scheme, no iterative computations are needed to achieve the final pressure and velocity corrections in the extended Direct-SIMPLE procedure, therefore extremely high computational efforts can be avoided. Using three different types of model alloys, pseudo-binary In718 base-4.85 wt% Nb, γ(TiAl)-55 at% Al and Al-4.5 wt% Cu systems, sample computations for solving strongly coupled solidification transport phenomena in directionally solidifying shaped castings under static and harmonic EM-fields of different strengths are carried out, to demonstrate the feasibility and efficient calculation performance of the present model and numerical methods. Copyright © 2004 John Wiley & Sons, Ltd.

KEY WORDS: extended Direct-SIMPLE scheme; continuum model; primitive variable form; electromagnetic-/gravity-/solidification-shrinkage-driven flow; solidification transport phenomena; directional solidification of shaped alloy castings

INTRODUCTION

Electromagnetic (EM) techniques have been applied to materials processing and metallurgical processes since the past half century or so, and nowadays are showing wider application

*Correspondence to: D. Xu, School of Materials Science and Engineering, Harbin Institute of Technology, P.O. Box 434, Harbin 150001, People's Republic of China.
†E-mail: damingxu@hit.edu.cn
‡E-mail: yunfeng_bai@163.com
§E-mail: guojj@hit.edu.cn

Contract/grant sponsor: National Key Project; contract/grant number: 41318.4.2.9
Contract/grant sponsor: Key China NNSF; contract/grant number: 50395102

Received 16 November 2003
Revised 30 April 2004

backgrounds in materials processing, called electromagnetic processing of materials (EPM) [1–3]. A major field in EPM is in controlled solidification processes of metallic alloy materials with various EM techniques applied. This can be seen in direct-chill (DC) casting, or continuous casting of Al alloy and steel ingots with alternating EM inductors or EM stirrers/brakes for meniscus shapes and melt flow controls [4–6], or with combined static and alternating EM fields applied for solidification structure refining [7].

In such EPM applications, magnetohydrodynamics (MHD) phenomena [1, 2, 5] play important roles in attaining the quality controls of the metallic alloy products, which in fact can be classified as special fluid flow phenomena in solidification processes under various EM fields or Lorentz forces applied. Therefore, for computer modelling of the heat energy, species mass and momentum transport processes in an alloy solidification system under an EM field, extra numerical solution efforts may need to account for such EM influences (namely the Lorentz forces). This is particularly important in achieving an efficient solidification transport phenomena/processes (STP) simulation because the numerical solution to the strongly pressure-linked liquid flow usually takes the greatest portion of the entire computational effort.

In a previous computer model for the transport phenomena in a binary dendrite solidification process based on a continuum formulation [8], the present authors proposed a numerical method for direct solution of strongly pressure-linked flow problems which are induced by both the gravity and solidification-shrinkage forces [9]. The aim of the present paper is to extend the continuum model and the corresponding numerical solution methods to a more general STP case that is under the influence of an arbitrary EM field. Example computations for the liquid flow behaviours under both the gravity and static/harmonic EM fields, and the heat and solute mass transfers in the solidification transport processes of shaped alloy castings will be performed to demonstrate the feasibility and computational efficiency of the extended solidification model and numerical methods.

MODEL AND NUMERICAL ALGORITHMS

EM solidification model

For a numerical description of macroscopic dendrite STP in alloy castings and ingots, it is convenient to adopt a continuum model to start the computer modelling [8, 10]. With the assumptions of

(1) the external forces involved in a solidifying system are gravity and Lorentz force;
(2) no pores will occur, i.e. the geometric continuity, $f_L + f_S = 1$, holds for any region in the casting/ingot domain;
(3) the solid phase is macroscopically static during solidification;
(4) local thermodynamic equilibrium holds at the microscopic solid–liquid interfaces;
(5) Newtonian and laminar liquid flow present; and
(6) the model alloy is a binary system;

the mathematical model for the present numerical modelling includes the following equations:

Solidification heat energy transfer:

$$\partial[(\rho c_P)_{\mathrm{m}}T]/\partial t + \nabla(f_{\mathrm{L}}\rho_{\mathrm{L}}c_{P\mathrm{L}}\mathbf{V}T) = \nabla[\lambda_{\mathrm{m}}\nabla T] + \rho_{\mathrm{S}}h(\partial f_{\mathrm{S}}/\partial t) + q_J \tag{1}$$

where the electromagnetically inducted Joule heat is given by

$$q_J = \mathbf{J}_G \cdot \mathbf{E} = \mathbf{J}_G^2/\sigma \tag{2}$$

Solidification solute mass transfer:

$$\partial(\rho C)_{\mathrm{m}}/\partial t + \nabla(f_{\mathrm{L}}\rho_{\mathrm{L}}\mathbf{V}C_{\mathrm{L}}) = \nabla[D_{\mathrm{L}}\nabla(f_{\mathrm{L}}\rho_{\mathrm{L}}C_{\mathrm{L}}) + D_{\mathrm{S}}\nabla(f_{\mathrm{S}}\rho_{\mathrm{S}}C_{\mathrm{S}})] \tag{3}$$

where [10]:

$$\partial(\rho C)_{\mathrm{m}}/\partial t = (\rho_{\mathrm{S}}C_{\mathrm{S}})^*\partial f_{\mathrm{S}}/\partial t + \Phi f_{\mathrm{S}}\partial(\rho_{\mathrm{S}}C_{\mathrm{S}})^*/\partial t + (\rho_{\mathrm{L}}C_{\mathrm{L}})\partial f_{\mathrm{L}}/\partial t + f_{\mathrm{L}}\partial(\rho_{\mathrm{L}}C_{\mathrm{L}})/\partial t \tag{4}$$

$$\Phi = \theta\varphi/(1+\theta\varphi)$$

$$\varphi = (D_{\mathrm{S}}(T)/R_f)\zeta \cdot \mathbf{A}_{2N}$$

$$\theta = k(1+\beta)f_{\mathrm{S}}/f_{\mathrm{L}}^2$$

Liquid–solid phase-change characteristic function for a specific binary alloy

$$T_{\mathrm{Liq}} = T_{\mathrm{Liq}}(C_{\mathrm{L}}^*) \tag{5}$$

Solidification mass conservation:

$$\partial\rho_{\mathrm{m}}/\partial t = -\nabla(f_{\mathrm{L}}\rho_{\mathrm{L}}\mathbf{V}) \tag{6}$$

where [11]:

$$\partial\rho_{\mathrm{m}}/\partial t \approx \rho_{\mathrm{S}}^*\partial f_{\mathrm{S}}/\partial t + \Phi f_{\mathrm{S}}\partial\rho_{\mathrm{S}}^*/\partial t + \rho_{\mathrm{L}}\partial f_{\mathrm{L}}/\partial t + f_{\mathrm{L}}\partial\rho_{\mathrm{L}}/\partial t \tag{7}$$

Momentum transfer for bulk/interdendritic liquid flow:

$$\partial(f_{\mathrm{L}}\rho_{\mathrm{L}}\mathbf{V})/\partial t + \nabla[(f_{\mathrm{L}}\rho_{\mathrm{L}}\mathbf{V})\cdot\mathbf{V}] = \nabla[\mu\nabla(f_{\mathrm{L}}\mathbf{V})] - \nabla(f_{\mathrm{L}}P) - (\mu f_{\mathrm{L}}^2/K)\mathbf{V} + \mathbf{F}_{\mathrm{B}} \tag{8}$$

For the present modelling, the body force term induced by external fields includes the gravity and Lorentz force:

$$\mathbf{F}_{\mathrm{B}} = f_{\mathrm{L}}\rho_{\mathrm{L}}\mathbf{g} + \mathbf{F}_{\mathrm{L}} \tag{9}$$

where the Lorentz force acting on the moving liquid phase during solidification can be further expressed as:

$$\mathbf{F}_{\mathrm{L}} = \sigma f_{\mathrm{L}}(\mathbf{E} + \mathbf{V}\times\mathbf{B})\times\mathbf{B} = f_{\mathrm{L}}\{\mathbf{J}_G\times\mathbf{B} + \sigma[(\mathbf{V}\cdot\mathbf{B})\mathbf{B} - \mathbf{B}^2\mathbf{V}]\} \tag{10}$$

In the above macroscopic solidification transport model, Equation (4) gives an expression for the time-differential mixture-averaged composition (TDMAC) term for a dendrite solidification process with any solid back-diffusion (SBD) inside the growing dendrites and with discretionary dendrite morphology. The non-dimensional parameters φ and θ represent a dendritic geometry-modified Fourier diffusion number and the sensibility of the interdendritic-liquid-concentration variation in response to (or, dendritic solidification-starting/ending effects

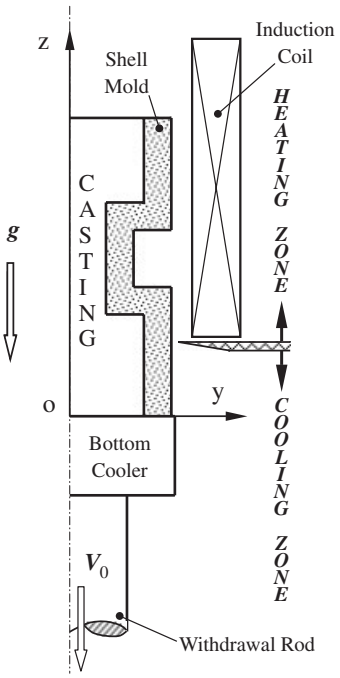

Figure 1. Schematic directional solidification configuration for a shaped alloy casting under an inducted EM field.

on) the SBD [10], respectively. Equation (7) was proposed with a similar microscopic modelling to Equation (4) for the time-differential mixture averaged density (TDMAD) term in the solidification mass-conservation equation (6) [11].

For the influences of EM-fields on the solidification transport processes, the extended continuum model of Equations (1)–(10) shows that the time- and position-dependent fields of magnetic flux density **B** and electromagnetically inducted current $\mathbf{J}_G$ in the alloy casting/ingot domain of interest need to be instantaneously determined. Maxwell's equations and the corresponding constitutive relationships for the related media including the moving alloy melts provide such mathematical equations, as those listed in Tables XV and XVI in Reference [12].

A two-dimensional (2-D) solidification configuration for shaped binary castings under an EM-field in the present model is shown in Figure 1. The blade-like alloy casting in a shell mould directionally solidifies upwards. The applied EM-field can be either transverse static ones of different strengths, or vertical harmonic of different frequencies and strengths inducted by coils that move upwards at a speed of V_0 relatively to the casting/shell mould/water cooler.

For a 2-D EM solidification transport problem in the y-o-z rectangular co-ordinates system depicted in Figure 1, the expressions for the Joule heat and Lorentz force, Equations (2) and (10), can be reduced to

$$q_J = J_{G|x}^2/\sigma \tag{11}$$

and

$$F_{\mathrm{L}|y} = f_{\mathrm{L}}\{-J_{G|x}B_z + \sigma[(\mathbf{V}\cdot\mathbf{B})B_y - \mathbf{B}^2 V_y]\} \tag{12}$$

$$F_{\mathrm{L}|z} = f_{\mathrm{L}}\{J_{G|x}B_y + \sigma[(\mathbf{V}\cdot\mathbf{B})B_z - \mathbf{B}^2 V_z]\} \tag{13}$$

respectively (for the present 2-D modelling case: $J_{G|y} = J_{G|z} \equiv 0$, $B_x \equiv 0$, $V_x \equiv 0$ and $F_{\mathrm{L}|x} \equiv 0$).

Numerical formulae and procedures for the model solution

The same 2-D meshing pattern and co-ordinate system for a casting/ingot domain as illustrated in Reference [13, Figure 2] is used for the present numerical approaches. The 2-D continuum model-based numerical formula for the heat energy transport for a control volume $[j,k]$ can be derived as

$$T_{j,k}^{i+1'} = \{\mathrm{TF0}\cdot T_{j,k}^{i} - \Delta t^{i+1}\{c_{p\mathrm{L}j,k}^{i}[(\mathrm{TVY1}-\mathrm{TVY2})/\Delta y_j + (\mathrm{TVZ1}-\mathrm{TVZ2})/\Delta z_k]$$
$$-[(\mathrm{TDY1}-\mathrm{TDY2})/\Delta y_j + (\mathrm{TDZ1}-\mathrm{TDZ2})/\Delta z_k] - q_J^{i+1}\}\}/\mathrm{TF1} \tag{14}$$

where the electromagnetically inducted Joule heat can be numerically calculated by:

$$q_J^{i+1} = (J_{G|x}^{i+1})^2/\sigma \tag{15}$$

The terms of TVY1, TVY2, TVZ1, TVZ2, TDY1, TDY2, TDZ1, TDZ2, TF0 and TF1 in Equation (14) take the same expression forms as those listed in Reference [13]. The latent heat release term for the liquid–solid phase change is temporally omitted in Equation (14) and will be numerically treated later by an iterative solution procedure for the instantaneous $T - f_{\mathrm{S}} - C_{\mathrm{L}}$ coupling. The adopted $T - f_{\mathrm{S}} - C_{\mathrm{L}}$ coupling solution method, previously proposed in Reference [13] has been recently extended to a more general solidification case to accommodate any microscopic SBD and dendrite morphologies [11, 14] and shown to be available and efficient for three-dimensional (3-D) [15], or multi-component [16] solidification cases. Furthermore, the temperature- and composition-dependent alloy properties for different phases in Equation (1), such as the specific heats, $c_{P\mathrm{L}}(T,C)/c_{P\mathrm{S}}(T,C)$, and the thermal conductivity, $\lambda_{\mathrm{m}}(T,C)$, etc, have been taken into account.

The 2-D numerical formula for the solidification solute mass transport, derived based on Equations (3) and (4) for the control volume $[j,k]$, has a similar expression form to Equation (9) of Reference [13] with the corresponding modifications for the solid diffusions [14].

Based on the same staggered control volumes as illustrated in Figure 2 of Reference [9] and similar discretization and formulation procedures, the numerical calculation equations for the 2-D momentum transports and mass continuity of the alloy melt flow during solidification under a magnetic field can be derived as follows:

Component of mass-flow in y direction

$$\mathrm{RFVY}_{j+1/2,k}^{i+1} = \{\mathrm{RFVY}_{j+1/2,k}^{i} - \Delta t^{i+1}[(\mathrm{VVY1}-\mathrm{VVY2}-\mathrm{VDY1}+\mathrm{VDY2}+\mathrm{VYP})/\Delta y_{j+1/2}$$
$$+(\mathrm{VVZ1}-\mathrm{VVZ2}-\mathrm{VDZ1}+\mathrm{VDZ2})/\Delta z_k + \mathrm{VYFL}]\}/\mathrm{VF1} \tag{16}$$

where

$$\mathrm{VYFL} = \{(f_{\mathrm{L}} J_{G|x} B_z)^{i+1/2} - [\sigma(f_{\mathrm{L}} V_y B_y + f_{\mathrm{L}} V_z B_z)]^i B_y^{i+1/2}\}_{j+1/2,k} \tag{17}$$

$$\mathrm{VF1} = 1 + \Delta t^{i+1}\{[(f_{\mathrm{L}}\mu)/K + \sigma(B_y^2 + B_z^2)]/\rho_{\mathrm{L}}\}_{j+1/2,k}^{i+1} \tag{18}$$

The terms of VVY1, VVY2, VVZ1, VVZ2, VDY1, VDY2, VDZ1, VDZ2 and VYP in Equation (16) have the same expression forms as those expressed in Reference [9].

Component of mass-flow in z direction

$$\begin{aligned}\mathrm{RFVZ}_{j,k-1/2}^{i+1} = \{&\mathrm{RFVZ}_{j,k-1/2}^{i} - \Delta t^{i+1}[(\mathrm{VVY3} - \mathrm{VVY4} - \mathrm{VDY3} + \mathrm{VDY4})/\Delta y_j \\ &+ (\mathrm{VVZ3} - \mathrm{VVZ4} - \mathrm{VDZ3} + \mathrm{VDZ4} + \mathrm{VZP})/\Delta z_{k-1/2} + \mathrm{VZG} + \mathrm{VZFL}]\}/\mathrm{VF2}\end{aligned} \tag{19}$$

where

$$\mathrm{VZFL} = -\{(f_{\mathrm{L}} J_{G|x} B_y)^{i+1/2} + [\sigma(f_{\mathrm{L}} V_y B_y + f_{\mathrm{L}} V_z B_z)]^i B_z^{i+1/2}\}_{j,k-1} \tag{20}$$

$$\mathrm{VF2} = 1 + \Delta t^{i+1}\{[(f_{\mathrm{L}}\mu)/K + \sigma(B_y^2 + B_z^2)]/\rho_{\mathrm{L}}\}_{j,k-1/2}^{i+1} \tag{21}$$

Again, the terms of VVY3, VVY4, VVZ3, VVZ4, VDY3, VDY4, VDZ3, VDZ4, VZP and VZG in Equation (19) take the same expression forms as those in Reference [9].

It should be noted that the numerical flow momentum formulae of Equations (16) and (19) take a semi-implicit finite-difference form. The numerical terms of pressure difference and Darcy resistance are set at the time level of t^{i+1}, in addition to the numerical Lorentz and gravity forces taken at time $t^{i+1/2}$ ($t^{i+1/2}$ time's gravity force is known at t^{i+1}), while the numerical convection and viscous diffusion terms are chosen at time t^i [9].

The solidification mass continuity Equation (6)/(7) is discretized into the following full-implicit numerical formula:

$$\begin{aligned}&[(\rho_{\mathrm{S}}^* \Delta f_{\mathrm{S}})_{j,k}^{i+1} + \Phi_{j,k}^i f_{\mathrm{S}j,k}^i(\rho_{\mathrm{S}j,k}^{*i+1} - \rho_{\mathrm{S}j,k}^{*i}) + (\rho_{\mathrm{L}} f_{\mathrm{L}})_{j,k}^{i+1} - (\rho_{\mathrm{L}} f_{\mathrm{L}})_{j,k}^{i}]\Delta y_j \Delta z_k / \Delta t^{i+1} \\ &\quad + \Delta z_k(\mathrm{RFVY}_{j+1/2,k}^{i+1} - \mathrm{RFVY}_{j-1/2,k}^{i+1}) + \Delta y_j(\mathrm{RFVZ}_{j,k-1/2}^{i+1} - \mathrm{RFVZ}_{j,k+1/2}^{i+1}) \\ &= 0 \quad (j,k = 1,2,3,\ldots)\end{aligned} \tag{22}$$

Decompose the relative pressure of t^{i+1} time in the numerical momentum Equations (16) and (19) into two terms, i.e. to be expressed as a sum of the relative pressure at time t^i and the pressure change in the time interval $\Delta t^{i+1}(= t^{i+1} - t^i)$:

$$(f_{\mathrm{L}} P)_{j,k}^{i+1} = (f_{\mathrm{L}} P)_{j,k}^{i} + \Delta(f_{\mathrm{L}} P)_{j,k}^{i+1} \tag{23}$$

Furthermore, separate the t^{i+1} time's superficial mass-flow-rates in y and z directions, $\mathrm{RFVY}_{j+1/2,k}^{i+1}$ and $\mathrm{RFVZ}_{j,k-1/2}^{i+1}$, into some approximate values, $\mathrm{RFVY}_{j+1/2,k}^{i+1^*}$ and $\mathrm{RFVZ}_{j,k-1/2}^{i+1^*}$,

and correction ones, $\mathrm{RFVY}^{i+1'}_{j+1/2,k}$ and $\mathrm{RFVZ}^{i+1'}_{j,k-1/2}$, respectively, i.e.

$$\mathrm{RFVY}^{i+1}_{j+1/2,k} = \mathrm{RFVY}^{i+1^*}_{j+1/2,k} + \mathrm{RFVY}^{i+1'}_{j+1/2,k} \tag{24}$$

$$\mathrm{RFVZ}^{i+1}_{j,k-1/2} = \mathrm{RFVZ}^{i+1^*}_{j,k-1/2} + \mathrm{RFVZ}^{i+1'}_{j,k-1/2} \tag{25}$$

In the present model, a similar mathematical treatment to that proposed in Reference [9, Equations (7″) and (12a)] is adopted, so that $\mathrm{RFVY}^{i+1^*}_{j+1/2,k}$ and $\mathrm{RFVZ}^{i+1^*}_{j,k-1/2}$ can have a definite physical meaning: they present the approximate superficial mass-flow-rates at t^{i+1} that are calculated by Equations (16) and (19), respectively, but using the t^i time's pressure field, $(f_{\mathrm{L}}P)^i_{j,k}$ $(j,k=1,2,3,\ldots)$, instead of the unknown pressure difference terms at t^{i+1}, VYP and VZP, and with the approximate terms of Darcy resistance and magnetic deceleration [12] due to the liquid flows of $\mathrm{RFVY}^{i+1^*}_{j+1/2,k}$ and $\mathrm{RFVZ}^{i+1^*}_{j,k-1/2}$ (see Equations (10), (18) and (21)). At the same time, the superficial mass-flow-rate corrections, $\mathrm{RFVY}^{i+1'}_{j+1/2,k}$ and $\mathrm{RFVZ}^{i+1'}_{j,k-1/2}$, can be explicitly determined by:

$$\mathrm{RFVY}^{i+1'}_{j+1/2,k} = -\Delta t^{i+1}[\Delta(f_{\mathrm{L}}P)^{i+1}_{j,k+1} - \Delta(f_{\mathrm{L}}P)^{i+1}_{j,k}]/(\Delta y_{j+1/2}\cdot \mathrm{VF1}_{j+1/2,k}) \tag{26}$$

$$\mathrm{RFVZ}^{i+1'}_{j,k-1/2} = -\Delta t^{i+1}[\Delta(f_{\mathrm{L}}P)^{i+1}_{j,k-1} - \Delta(f_{\mathrm{L}}P)^{i+1}_{j,k}]/(\Delta z_{k-1/2}\cdot \mathrm{VF2}_{j,k-1/2}) \tag{27}$$

Note that in Equations (26) and (27), the terms, $\mathrm{VF1}_{j+1/2,k}$ and $\mathrm{VF2}_{j,k-1/2}$, take the same forms as Equations (18) and (21), i.e. under the influences of both the Darcian and EM resistances [12].

Now, it is known that the t^{i+1} time's superficial mass-flow-rates must meet the solidification mass continuity equation at time t^{i+1} [9, 17], therefore, substitute Equations (24) and (25) into Equation (22) for $\mathrm{RFVY}^{i+1}_{j+1/2,k}$ and $\mathrm{RFVZ}^{i+1}_{j,k-1/2}$, respectively, and then Equation (22) changes into:

$$\begin{aligned}&\Delta z_k(\mathrm{RFVY}^{i+1'}_{j+1/2,k} - \mathrm{RFVY}^{i+1'}_{j-1/2,k}) + \Delta y_j(\mathrm{RFVZ}^{i+1'}_{j,k-1/2} - \mathrm{RFVZ}^{i+1'}_{j,k+1/2})\\ &\quad = -\mathrm{RES}^{i+1}_{j,k} \quad (j,k=1,2,3,\ldots)\end{aligned} \tag{28}$$

where

$$\begin{aligned}\mathrm{RES}^{i+1}_{j,k} = {}&[(\rho^*_{\mathrm{S}}\Delta f_{\mathrm{S}})^{i+1}_{j,k} + \Phi^i_{j,k} f^i_{\mathrm{S}j,k}(\rho^{*i+1}_{\mathrm{S}j,k} - \rho^{*i}_{\mathrm{S}j,k}) + (\rho_{\mathrm{L}} f_{\mathrm{L}})^{i+1}_{j,k} - (\rho_{\mathrm{L}} f_{\mathrm{L}})^i_{j,k}]\Delta y_j \Delta z_k/\Delta t^{i+1}\\ &+ \Delta z_k(\mathrm{RFVY}^{i+1^*}_{j+1/2,k} - \mathrm{RFVY}^{i+1^*}_{j-1/2,k}) + \Delta y_j(\mathrm{RFVZ}^{i+1^*}_{j,k-1/2} - \mathrm{RFVZ}^{i+1^*}_{j,k+1/2})\end{aligned} \tag{29}$$

represent mass residuum produced by only putting the approximate superficial mass-flow-rates, $\mathrm{RFVY}^{i+1^*}_{j+1/2,k}$ and $\mathrm{RFVZ}^{i+1^*}_{j,k-1/2}$, into Equation (22), which reflects the extent of meeting the mass continuity equation with these approximate velocity components. Refer to the Equations (24) and (25) with mathematical treatment similar to that of Reference [9], Equations (28) and (29) clearly indicate that these mass residuum should and can be fully balanced by the mass-

flow-rate corrections, $\mathrm{RFVY}^{i+1'}_{j+1/2,k}$ and $\mathrm{RFVZ}^{i+1'}_{j,k-1/2}$. Finally, substitute Equations (26) and (27) into Equation (28), the linear equations for the pressure change field during the time increment Δt^{i+1} are obtained as follows:

$$a^{i+1}_{j,k}\Delta(f_{\mathrm{L}}P)^{i+1}_{j,k} - a^{i+1}_{j-1/2,k}\Delta(f_{\mathrm{L}}P)^{i+1}_{j-1,k} - a^{i+1}_{j+1/2,k}\Delta(f_{\mathrm{L}}P)^{i+1}_{j+1,k} - a^{i+1}_{j,k+1/2}\Delta(f_{\mathrm{L}}P)^{i+1}_{j,k+1} - a^{i+1}_{j,k-1/2}\Delta(f_{\mathrm{L}}P)^{i+1}_{j,k-1} = b^{i+1}_{j,k} \quad (j,k=1,2,3,\ldots) \tag{30}$$

where the corresponding coefficients can be written as

$$a^{i+1}_{j-1/2,k} = \Delta z_k/\{\Delta y_{j-1/2}\{1+\Delta t^{i+1}\{[(f_{\mathrm{L}}\mu)/K+\sigma(B_y^2+B_z^2)]/\rho_{\mathrm{L}}\}^{i+1}_{j-1/2,k}\}\}$$

$$a^{i+1}_{j+1/2,k} = \Delta z_k/\{\Delta y_{j+1/2}\{1+\Delta t^{i+1}\{[(f_{\mathrm{L}}\mu)/K+\sigma(B_y^2+B_z^2)]/\rho_{\mathrm{L}}\}^{i+1}_{j+1/2,k}\}\}$$

$$a^{i+1}_{j,k+1/2} = \Delta y_j/\{\Delta z_{k+1/2}\{1+\Delta t^{i+1}\{[(f_{\mathrm{L}}\mu)/K+\sigma(B_y^2+B_z^2)]/\rho_{\mathrm{L}}\}^{i+1}_{j,k+1/2}\}\}$$

$$a^{i+1}_{j,k-1/2} = \Delta y_j/\{\Delta z_{k-1/2}\{1+\Delta t^{i+1}\{[(f_{\mathrm{L}}\mu)/K+\sigma(B_y^2+B_z^2)]/\rho_{\mathrm{L}}\}^{i+1}_{j,k-1/2}\}\}$$

$$a^{i+1}_{j,k} = a^{i+1}_{j-1/2,k} + a^{i+1}_{j+1/2,k} + a^{i+1}_{j,k+1/2} + a^{i+1}_{j,k-1/2}$$

$$b^{i+1}_{j,k} = -\mathrm{RES}^{i+1}_{j,k}/\Delta t^{i+1}$$

Like many other engineering problems, the set of linear Equations (30) has a coefficient matrix containing sparse elements. However, an important characteristic of this coefficient matrix that should be pointed out is that all the initially non-zero elements will change significantly with the solidification proceeding in an alloy ingot/casting domain. This is primarily caused by the Darcian resistances in the varying mushy (i.e. S+L) region. In the linear equation matrix, an off-diagonal coefficient corresponds to a staggered control volume, e.g. $a^{i+1}_{j-1/2,k} \Leftrightarrow$ volume $[j-1/2,k]$. The Darcian resistance term, i.e. $(f_{\mathrm{L}}\mu)/(K\rho_{\mathrm{L}})$, in such an off-diagonal coefficient can take a value from zero when the control volume is initially in a pure liquid state, to approaching infinity when the volume is nearly completely solidified, which in turn leads this coefficient to take a small value $\rightarrow$ zero.

Similarly, for a casting/ingot solidification case under a very strong EM-field, the coefficient matrix of Equations (30) may become even more difficult to numerically solve. Generally speaking, in an alloy solidification process, each part (each control volume) of the shaped casting/ingot will solidify at different times, and an EM-field, especially inducted by an alternating current, may be highly uneven. Through the numerical sample computations for 2-D solidification transport processes in various shaped castings and ingots (zero EM-field) implemented in References [9, 11, 13, 14, 16, 18] etc, it has been shown that an under-relaxation Gauss–Seidel algorithm is a convenient method to numerically solve the relevant linear equations similar to Equations (30). In the present work, the same method will be adopted to solve the Equations (30) for the solidification transport processes under different EM-fields.

RESULTS AND DISCUSSIONS

Comparison of the present V-P numerical solution scheme with SIMPLE method

To show the advantages and performance of the present numerical solution method described in the previous section, the authors' algorithm is compared with the SIMPLE scheme, which was proposed in the early 1970s [17, 19], and is widely used for solving the pressure-linked velocity problem in a fluid system. First, it should be pointed out that derivation of the present V-*P* coupling solution scheme starts with the same numerical treatment techniques as in SIMPLE method. Both the numerical methods separate the pressure and flow velocity at a new time level of t^{i+1} into some approximate values and corrections as a basic procedure for the numerical solution, in primitive variable forms, to the pressure-linked momentum transfer and mass continuity equations.

However, through the present numerical-solution scheme derivation, all the separated parts of the pressure and mass-flow-rate components at a new time t^{i+1} in Equations (23)–(25), have the distinct physical definitions, in particular the explicit mass-flow-rate corrections, i.e. Equations (26) and (27), are given. The importance of the derived mass-flow-rate correction formulae of Equations (26) and (27) is that, unlike in the SIMPLE scheme [17], no iterative computations will be required for the velocity corrections or the new relative pressure at t^{i+1} (Equation (23)), if the pressure change field in the time increment Δt^{i+1}, $\Delta(f_L P)_{j,k}^{i+1}$ $(j,k = 1,2,3,\ldots)$, is known, so that extremely high computational efforts can be avoided, especially for a 3-D solidification case with small mesh sizes. Through solving the linear algebraic Equations (30), the pressure change field during the time of Δt^{i+1} can be directly determined, as a result, the final (numerically accurate) relative pressure and velocity fields at the new time t^{i+1} can be immediately achieved using the Equations (23)–(27).

Furthermore, the present numerical method is fully available for solving a heat, mass and momentum transfer problem in a fluid system that the SIMPLE scheme can do [17, 19], but with high numerical solution efficiency. This can be easily seen by simply setting the liquid volume fraction $f_L(t,x,y,z) \equiv 1$ and the EM-field $\mathbf{B}(t,x,y,z) \equiv 0 / \mathbf{J}_G(t,x,y,z) \equiv 0$ in the present solidification model of Equations (1)–(10), and all the corresponding numerical Equations (14)–(30) (i.e. no solidification allowed and no EM-field applied) for the entire transport domain of interest.

Finally, in the present numerical scheme, although the mass continuity Equation (6)/(7) is discretized into a fully implicit finite-difference form, i.e. Equation (22), the numerical formulae derived for solving the *P*ressure-*L*inked mass-flow-rate *E*quation (8), i.e. Equations (16)–(21), are *S*emi-*IM*plicit ones, as pointed out in the previous section. Therefore, the present numerical algorithm may be named as a direct-SIMPLE method with extensions to account for dendrite solidification processes (varying Darcian resistances from the growing dendrite network) and EM-field influences, or 'extended Direct-SIMPLE' for short.

Sample computations

For the EM directional solidification configuration of shaped alloy castings schematically illustrated in Figure 1, three groups of sample simulations for the solidification transport phenomena under different EM-fields are presented to demonstrate the feasibility and performances of the present extended direct-SIMPLE algorithm. In the following computation examples, three different types of alloys, i.e. pseudo-binary In718 base-4.85 wt% Nb [20],

Table I. Initial and technological parameters for the present example simulations.

Alloys	In718 base-4.85 wt% Nb	γ(TiAl)-55 at% Al	Al-4.5 wt% Cu
Pouring temperature, T_P	1450°C	1500°C	700°C
Initial mould temperature, T_M	1500°C	1550°C	700°C
Heating zone temperature, T_h	1600°C	1600°C	950°C
Cooling zone temperature, T_C	45°C	45°C	25°C
Bottom cooler temperature, T_{BC}	45°C	45°C	25°C
Withdrawal velocity, V_0	0.15 mm/s	0.15 mm/s	0.15 mm/s

Al-4.5 wt% Cu and γ(TiAl)-55 at% Al are used as the modelling alloys. In the former two alloys, the solute Nb and Cu have higher densities than that of their base alloys, respectively, and in γ(TiAl)-55.0 at% Al binary alloy the Al solute is lighter than the stoichiometric γ(TiAl)-phase. The shell moulds for the three alloys are all made of CaO. The STP-related temperature/composition-dependent properties used for the present modelling alloys are same as those listed in References [11, 21, 22]. Table I gives a list of the initial and technological parameters for the present example simulations.

The mesh pattern for a half of shaped casting and one side of the shell mould as illustrated in Figure 1 is the same as that shown in Reference [11] with 1680 and 936 meshed elements for the casting and mould domains, respectively. All the alloy melted in the casting domains are assumed to be static and of uniform temperature at the start of withdrawal and cooling. The numerical computations for the field evolutions of temperature, concentration, solid-volume fraction, liquid pressure and flow velocity vectors, etc in the EM directional solidification processes of the shaped castings are implemented by a PC computer-based code [11], which has been further revised for the present work. The magnetic flux density $\mathbf{B}$ and inducted current $\mathbf{J}_G$ in the alloy casting/ingot domains are calculated using ANSYS 6.1 software.¶ The FEM analysis results of $\mathbf{B}$ and $\mathbf{J}_G$ output from ANSYS 6.1 are converted into FDM-formatted data files that can be read as input data by the authors' computation program for the present FDM-based STP simulations [22].

A full set of simulated results for the major fields involved in an EM directional solidification transport process of a shaped alloy casting is shown in Figure 2. These calculated results for the pseudo-binary In718 base-4.85 wt% Nb alloy solidified under a harmonic EM-field (2×10^4 Hz, 1×10^4 A t) at 10.06 s include the converted magnetic flux density vectors from the ANSYS-FEM analysis, the calculated Lorentz force vectors and its y-/z-component contours, contours of inducted Joule heat, velocity vectors and contours of relative pressure in liquid phase, and distributions of isosolid-volume fraction, isotherm and liquid isoconcentration. Due to the relatively high frequency of the alternating EM-field inducted in the solidifying casting, a skin-effect [12] for both the inducted magnetic flux density and Joule heat occurs, especially in the surface region of the lower block part of casting, see Figures 2(a) and 2(e). These phenomena in turn induce much larger Lorentz forces and liquid circulation velocities in the lower surface layer than any other region, Figures 2(b) and 2(f). Furthermore, due to

¶ANSYS is a trademark of ANSYS, Inc., Pittsburgh, U.S.A.

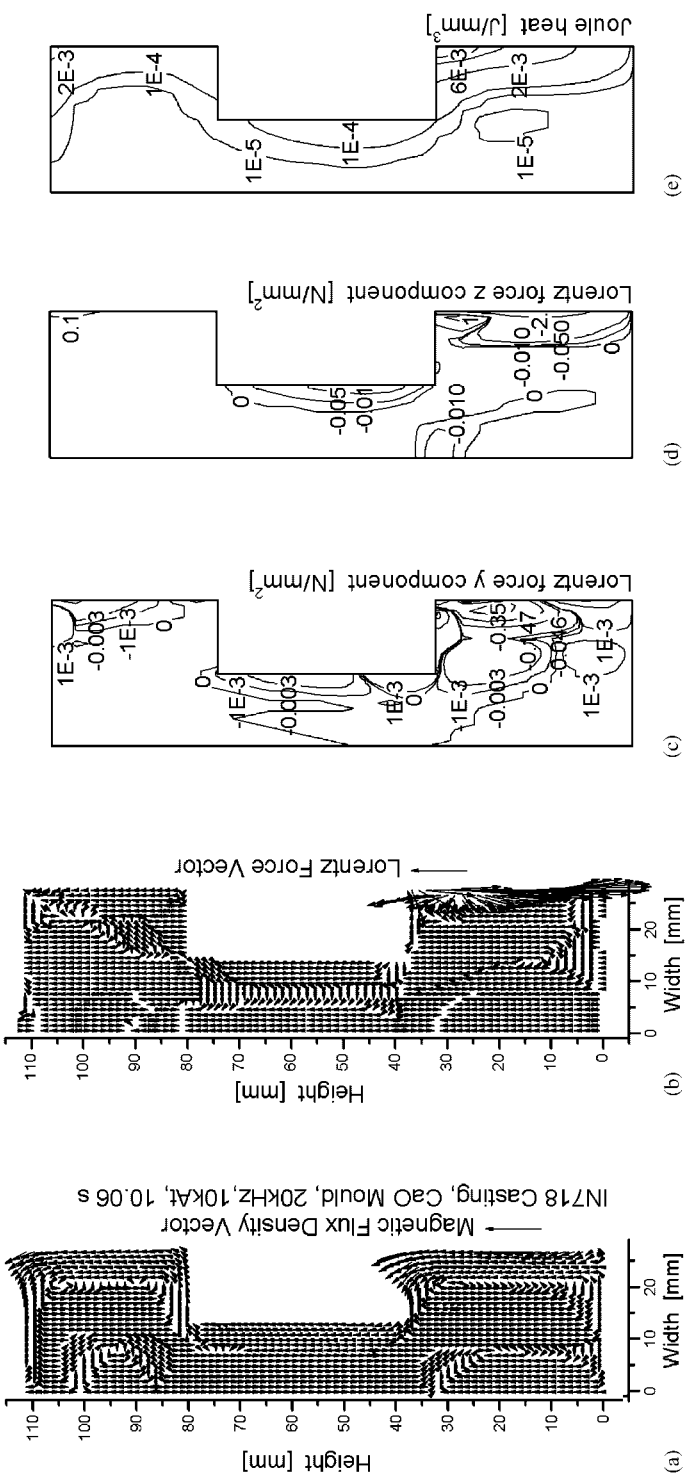

Figure 2. Calculated directional solidification transport phenomena of an In718 shaped casting under a harmonic EM field (20 kHz, 10 kA t) at 10.06 s: (a) FDM-formatted magnetic flux density vectors converted from the FEM-results of ANSYS 6.1; (b) Lorentz force vectors; (c) y-component of the Lorentz force; (d) z-component of the Lorentz force; (e) contours of inducted Joule heat; (f) velocity vectors of the alloy melt; (g) contours of relative pressure in liquid phase; (h) contours of solid volume fraction; (i) contours of temperature; (j) contours of liquid concentration of solute Nb (wt%).

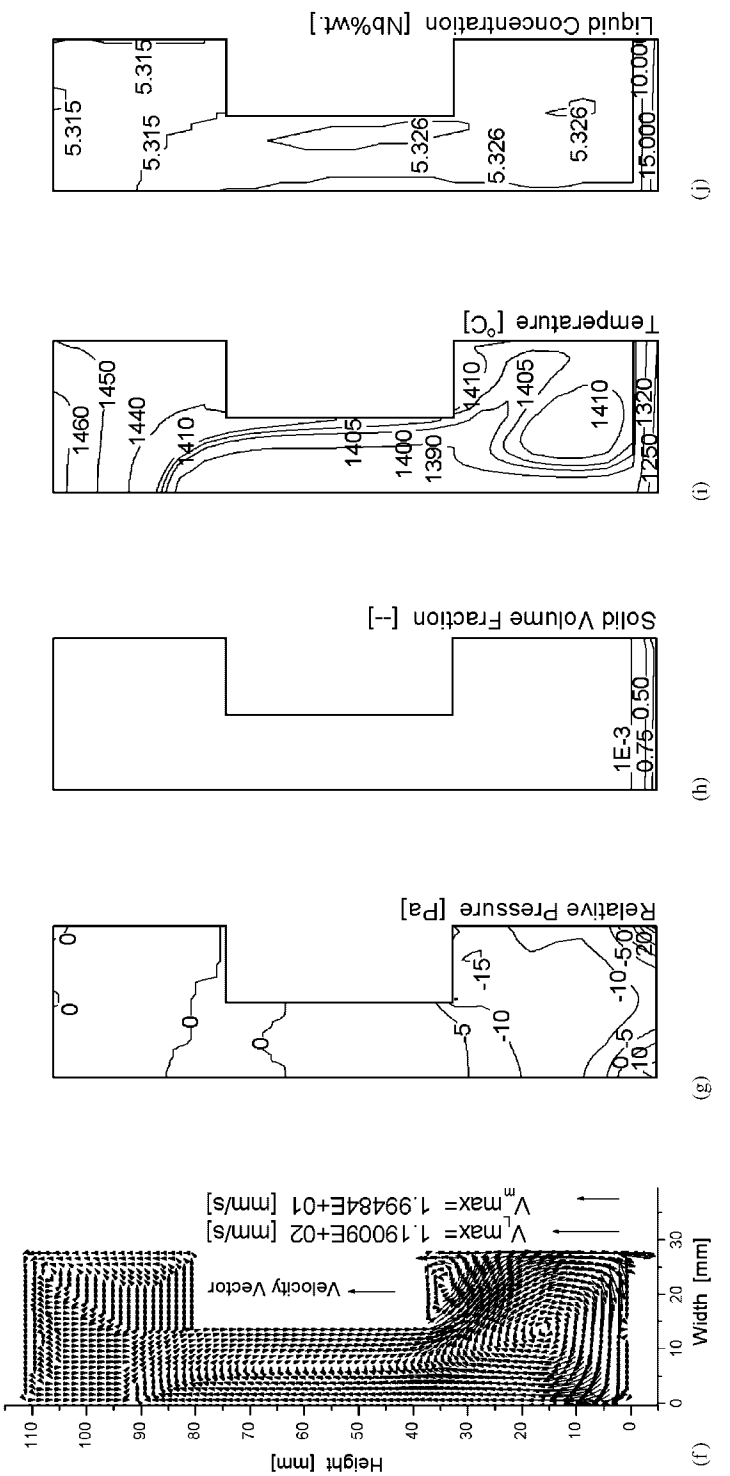

Figure 2. *Continued.*

the very fast circulation in the lower block bottom (there are two opposite rotating directions), some negative pressures holes form there, see Figure 2(g). The isotherm and isoconcentration lines are also led to approximately follow the liquid streamlines, Figures 2(i) and 2(j), except in the solidification region as described in Figure 2(h). In the solidification region, the solute concentration of the interdendritic liquid can rise as high as 15 wt% Nb because its partition coefficient is less than unity.

One of the important interactions between an applied magnetic field and a moving alloy melt is flow suppression or EM brake (EMBR) [1, 12]. This EMBR effect can be explicitly and primarily expressed by the last term on the far right-hand side of Equation (10), i.e. $-f_L\sigma(\mathbf{B}^2\mathbf{V})$ term (from which it can be seen that the EMBR force is primarily proportional to $Re(\mathbf{B}\cdot\mathbf{B}^*)$ and to $\mathbf{V}$, respectively). Figure 3 shows a group of simulation results to demonstrate such EMBR effects on the alloy melt flow in solidification processes. In the directional solidification case shown by Figure 3 for an Al-4.5% Cu shaped casting, a transverse static magnetic field of different strengths, 0, 500, 10^3, 2.5×10^3 and 10^4 A t, is applied. The calculation results for the flow velocity vectors, the relative pressure distribution in the liquid phase, the isosolid-volume fraction distribution, and contours of temperature shown in Figure 3 are all at a cooling/solidification time of 21.0 s. At this moment, about two thirds of the bottom block of the shaped casting is in a solid–liquid coexisting state (i.e. S+L zone).

In Figure 3, the simulated results with the zero magnetic field applied represent the directional solidification case that occurs only under downward gravity. It can be seen that, under this condition, several natural convection loops exist in the pure liquid region of the solidifying casting, and a downward interdendritic feeding flow occurs in the S+L region [9, 18]. The maximum velocities of these two kinds of liquid flow are 3.13 and 5.67×10^{-2} mm/s, respectively; see Figure 3(a), the 0 A t case. The corresponding relative pressure distribution is shown in Figure 3(b) of 0 A t case, from which it can be seen that the pressure variation in the pure liquid region is pretty small because the natural convection there is weak. However, in its S+L region, the liquid pressure changes from $\sim$0 Pa downward to about -5000 Pa. This large pressure gradient is necessary to drive the interdendritic liquid phase to overcome the Darcian resistance for feeding the solidification shrinkage occurring over the entire wide S+L region [9], even though the feeding flow velocity is quite low.

When the strength of the applied static magnetic field increases from 0 A t continuously to 10^4 A t, from Figure 3(a) it can be seen that remarkable EMBR effects on the natural convection in the pure liquid region of the directionally solidifying casting takes place. The maximum velocity of the natural convection decreases gradually from 3.13 mm/s for the zero magnetic case to 0.354 mm/s for the case of 10^4 A t magnetic field applied, i.e. almost a decrease of one order of magnitude. However, it is interesting to see that, no matter how strong the static magnetic field is applied, the velocity magnitude of the interdendritic-liquid feeding flow in the solidification region basically remains the same. This phenomenon, along with the large pressure gradients exhibited in the S+L region of Figure 3(b), implies that solidification shrinkage can act as a very strong inner force. From Figure 3(a) it also can be seen that, when the applied magnetic strength higher than $\sim$2500 A t, the natural convection basically has been completely suppressed. Instead, the flow in the pure liquid region is driven only by the solidification shrinkage that occurs in the S+L region, in order to meet the mass conservation for the entire solidifying casting domain, as described by

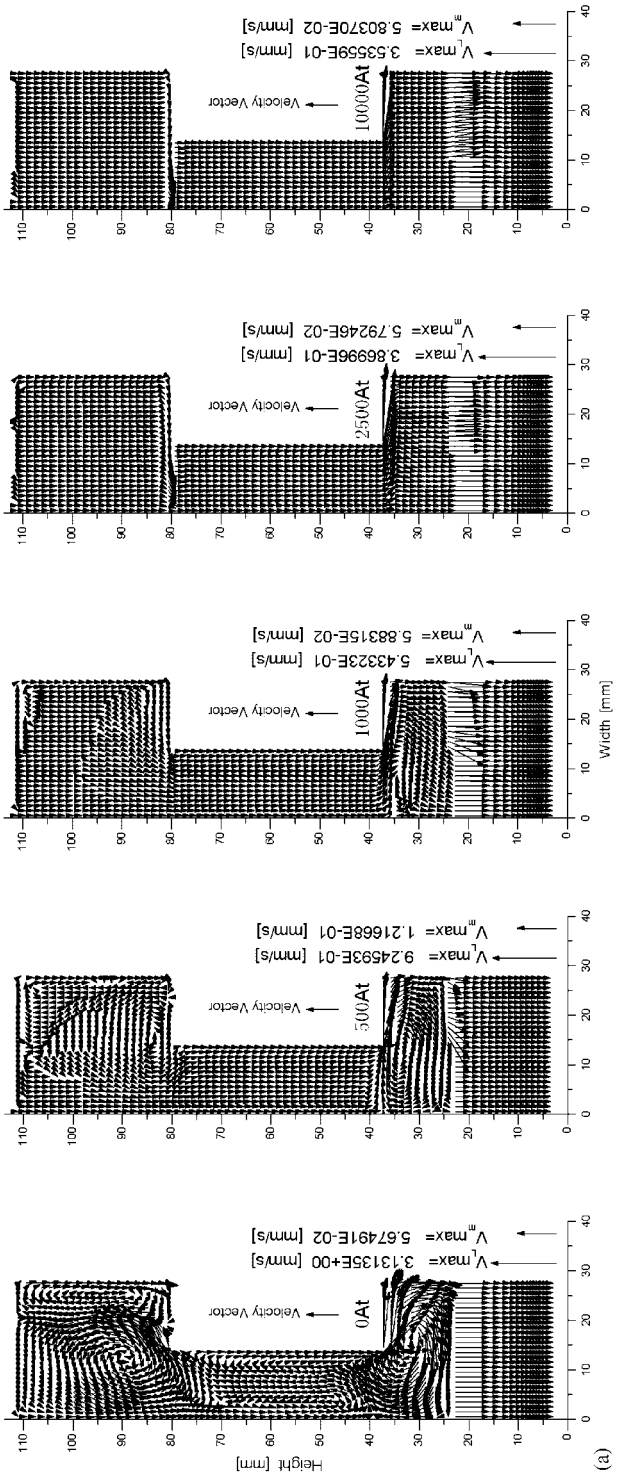

Figure 3. Comparisons of liquid flow and directional solidification behaviours of A1-4.5% Cu shaped casting under static magnetic fields inducted by different current-turns at $t = 21.0$ s: (a) velocity vectors of liquid phases; (b) contours of relative pressure in the liquid; (c) contours of solid volume fraction; (d) contours of temperature.

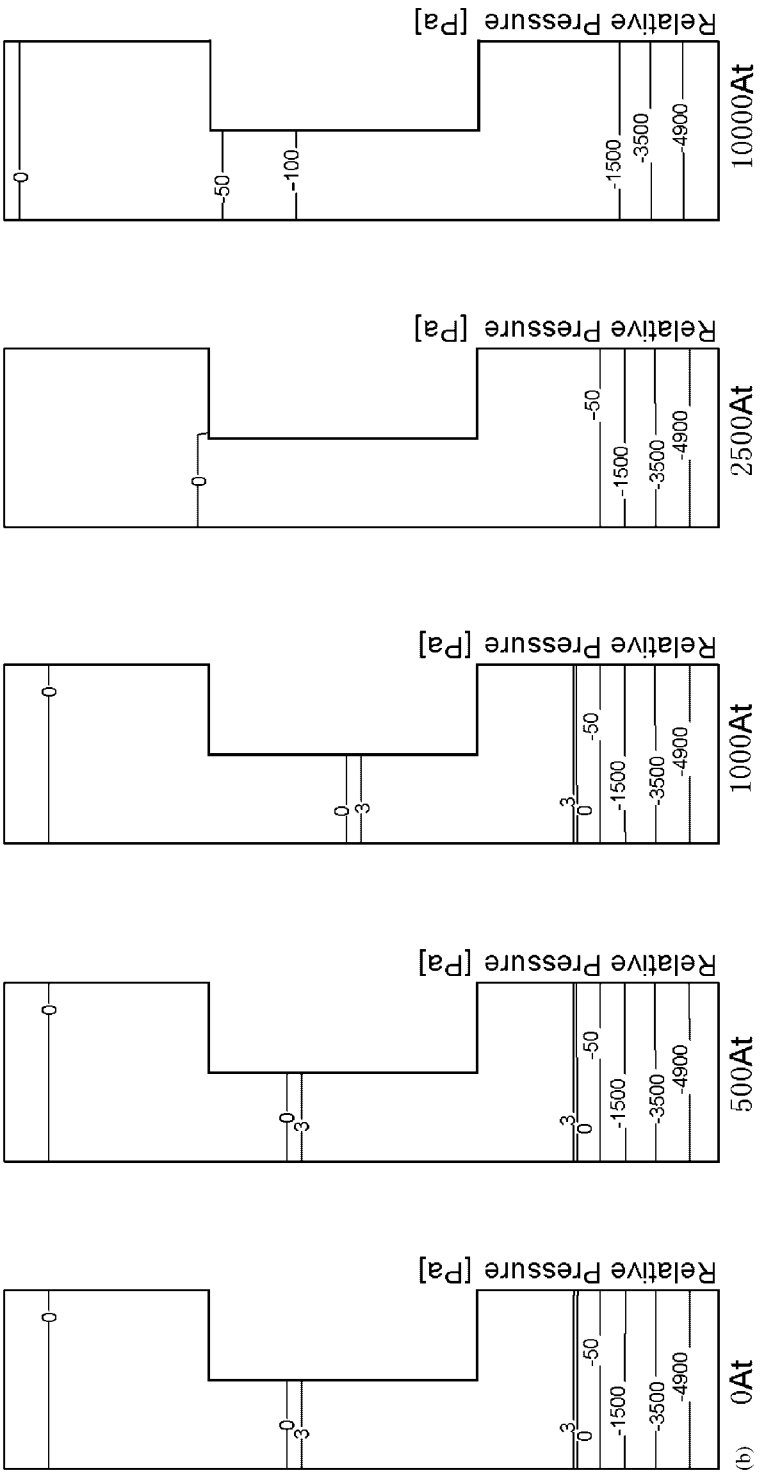

Figure 3. *Continued.*

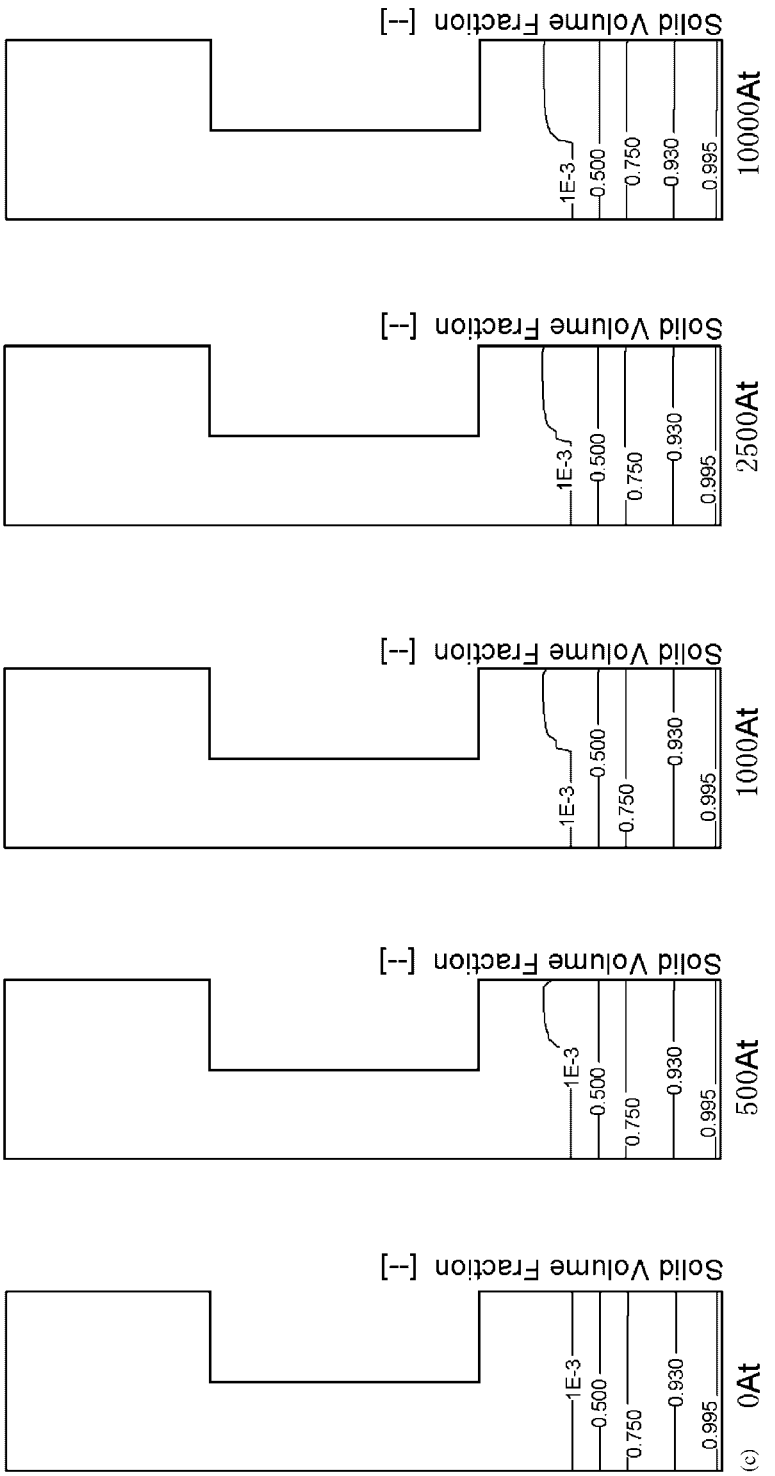

Figure 3. *Continued.*

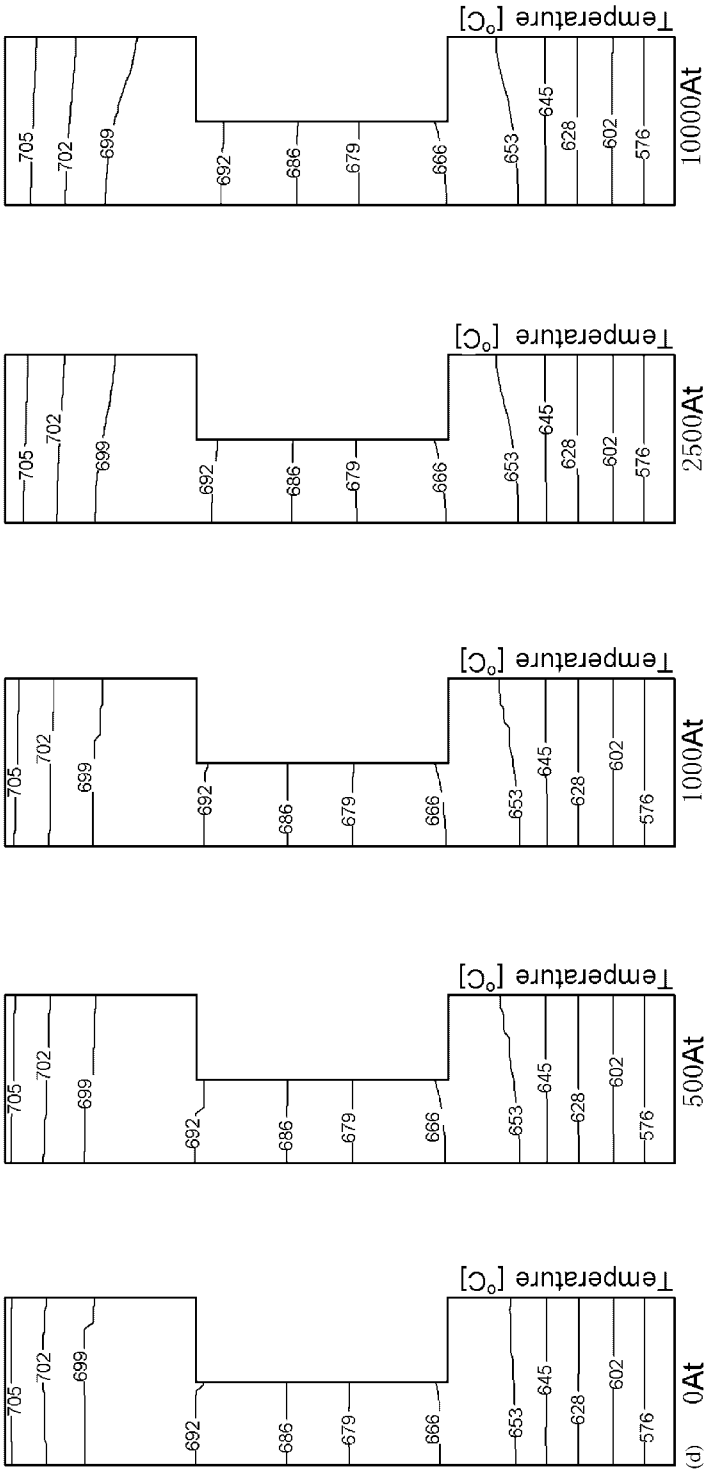

Figure 3. *Continued.*

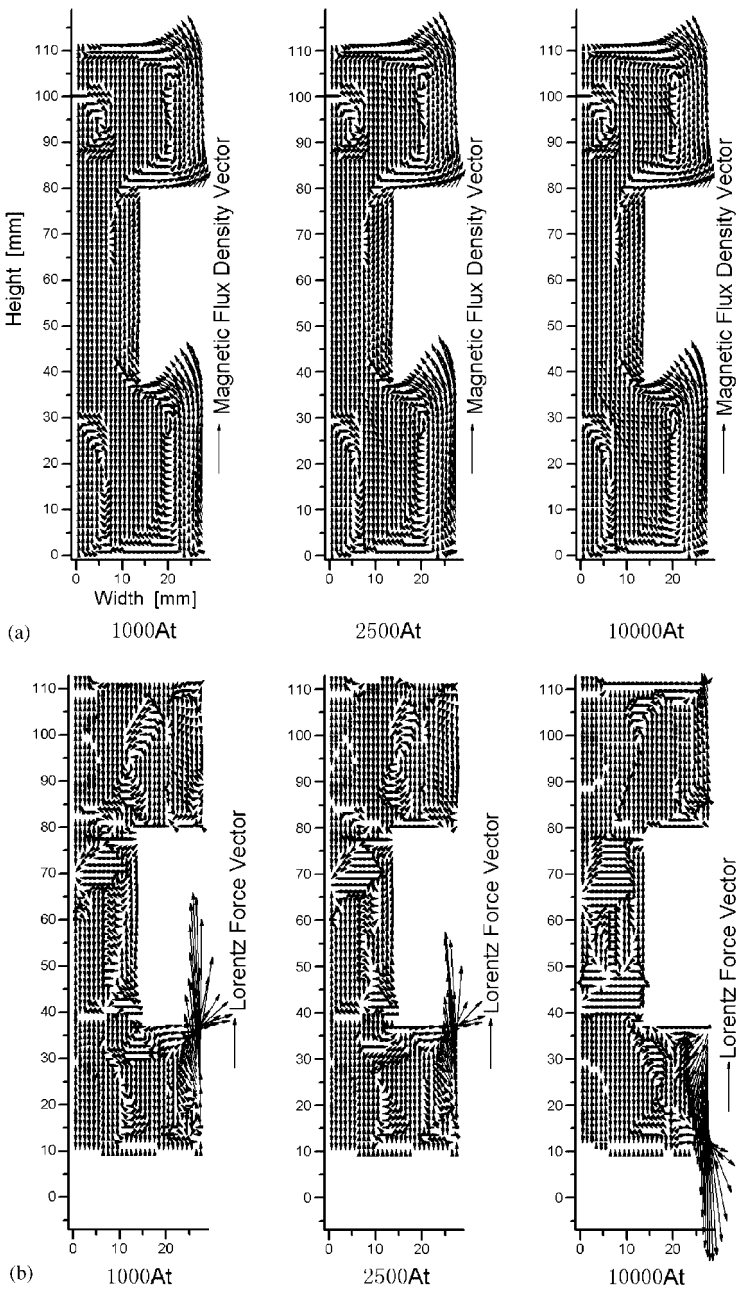

Figure 4. Comparison of the directional solidification transport behaviours of γ(TiAl)-55 at% Al shaped casting under harmonic magnetic fields inducted by different current-turns (20 kHz) at $t = 21.0$ s: (a) converted magnetic flux density vectors; (b) Lorentz force vectors; (c) velocity vectors; (d) contours of relative pressure; (e) contours of Joule heat; (f) contours of solid volume fraction; (g) contours of temperature; (h) contours of liquid concentration.

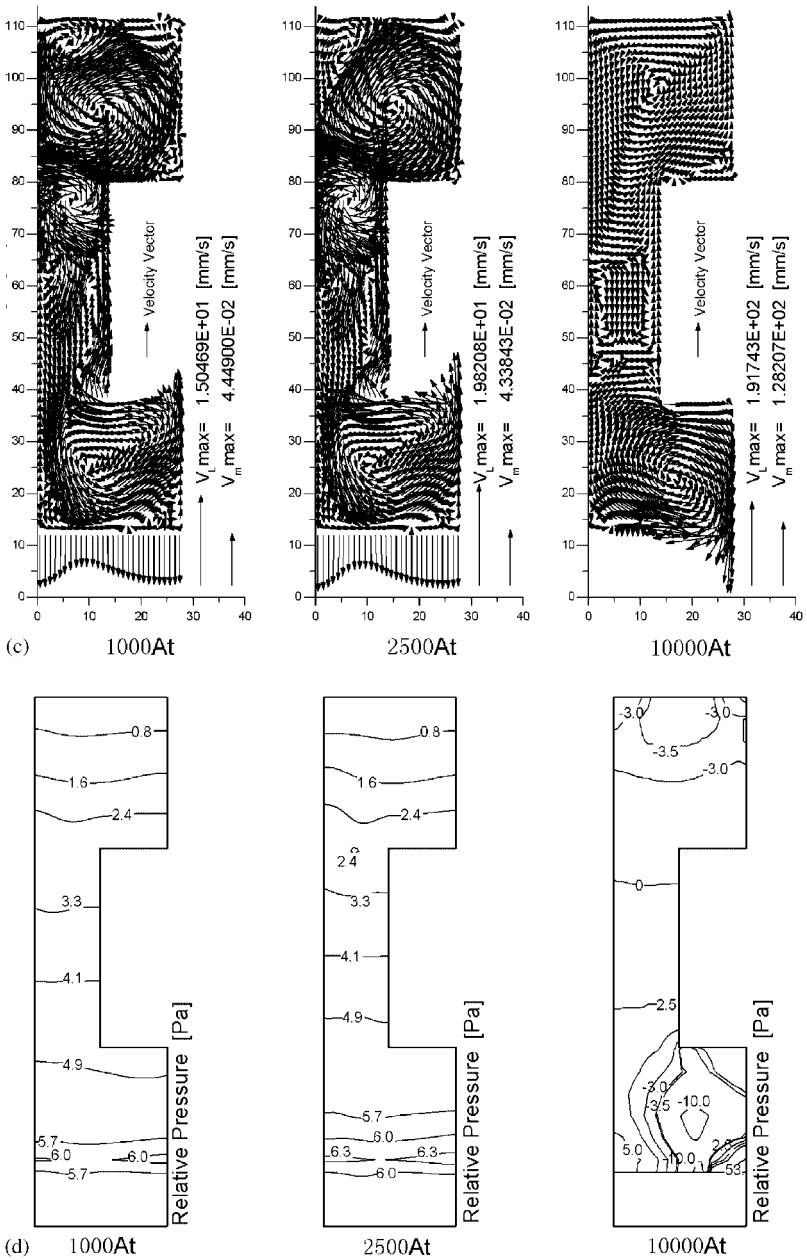

Figure 4. *Continued.*

Equation (6)/(7). Due to the highly weakened liquid flow in the pure liquid region with the much stronger static magnetic field applied, the heat transfer as well as the directional solidification pattern in the casting domain approaches a pure heat conduction type, see Figures 3(d) and 3(c).

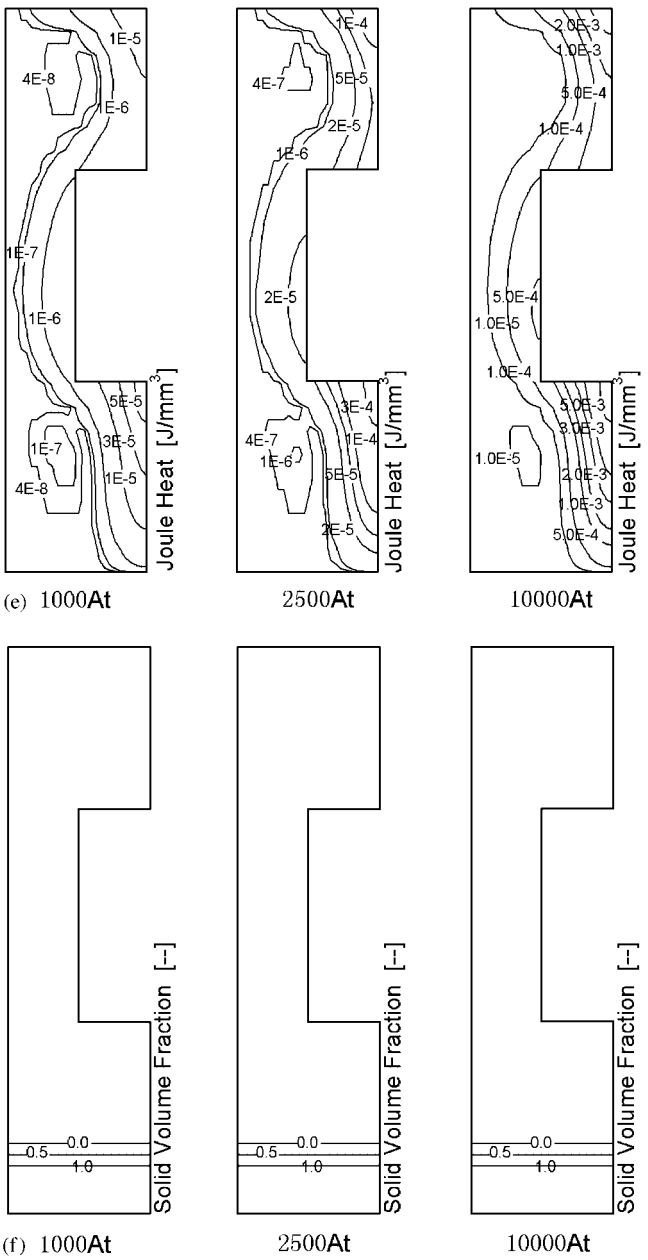

Figure 4. *Continued.*

On the right-hand sides of Equation (10), the first term in the Lorentz force expression, i.e. $f_L \sigma \mathbf{E} \times \mathbf{B}$ or $f_L \mathbf{J}_G \times \mathbf{B}$, represents the EM force component that is generated by the interaction between the inducted alternating current and the applied magnetic field. The function of this induced Lorentz force part is to drive a metallic melt tending to flow in the same direction

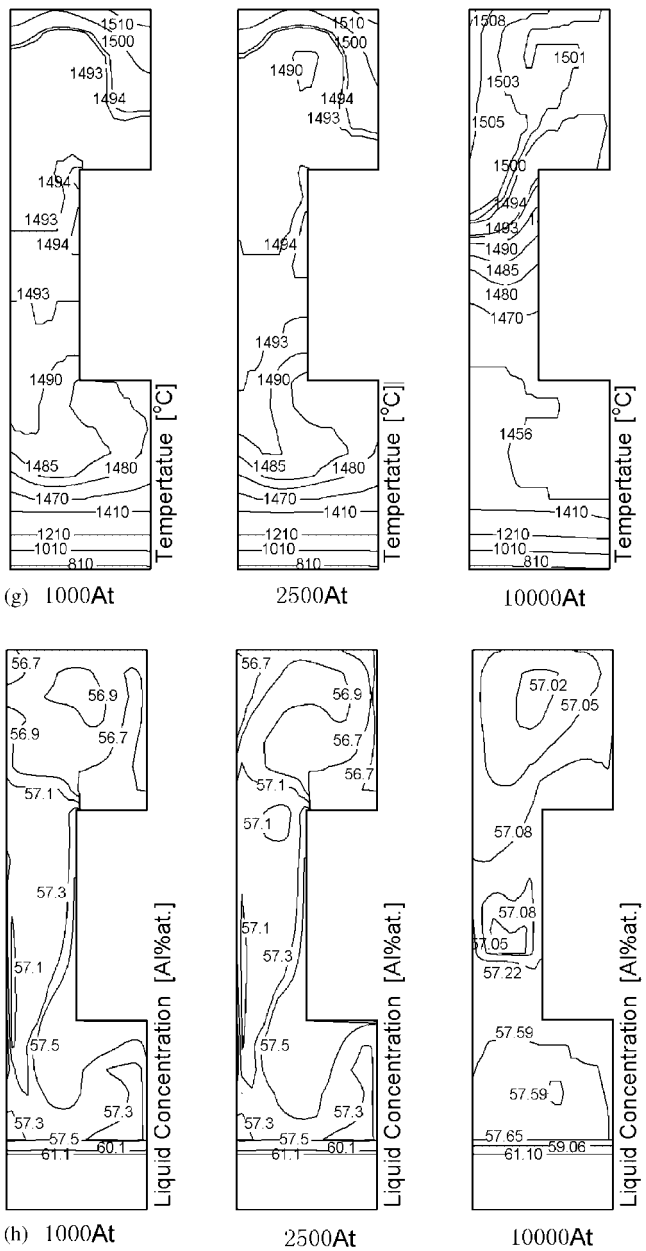

Figure 4. *Continued.*

of this Lorentz force part [1, 12]. Obviously, this part of the Lorentz force is proportional to both the strengths of the applied EM-field and its inducted current. To further demonstrate the numerical modelling ability of the proposed model and numerical solution methods, Figure 4 gives another group of calculation results for the directional solidification transport phenomena

of a shaped alloy casting but under a harmonic alternating EM-field of different strengths. The results are at a cooling/solidification time of 21.0 s and the model alloy for this simulation group is the γ(TiAl)-55 at% Al pseudo-binary system with a less dense solute of aluminium.

Figure 4(a) shows that the converted harmonic magnetic flux density vectors inducted in the directionally solidifying casting domains from the ANSYS-FEM analysis results with sinusoidal alternating currents of 10^3, 2.5×10^3 and 10^4 A t applied at a frequency of 2×10^4 Hz. It can be seen that, although these magnetic flux density vectors have different strengths they show the same distribution pattern. In Figure 4(e), the Joule heats inducted in the casting exhibit similar distribution behaviours, i.e. with similar contour curves but of higher values for higher current-loads applied. However, the corresponding Lorentz forces show some dissimilar distributions: for an even higher current-turns load applied the maximum EM forces induced in the surface layer of the lower casting block change their acting directions, see Figure 4(b). This phenomenon may be caused by the unsteady behaviours of the forced melt convections in the liquid region. From Figure 4(c) it also can be seen that, when the applied current-load increases from 2.5×10^3 to 10^4 A t, the induced maximum flow magnitude enhances from 19.8 to 191.7 mm/s. This very fast rotating convection in turn leads to a negative pressure hole in the lower block part of the casting, see Figure 4(d) of 10^4 A t case. The corresponding contours of solid-volume fraction, temperature and liquid concentration of solute Al are shown in Figures 4(f), 4(g) and 4(h), respectively.

Finally, it should be mentioned that all the above three groups of sample computations are implemented on PC computers using the authors' computer codes, and took a relatively short CPU-time to finish the numerical simulation for an entire directional solidification transport process under an EM-field. For example, on a PC computer equipped with a 2.4 GHz CPU, about 35 min CPU-times are required to finish the computations for a whole 229 s directional solidification process of an Al-4.5% Cu shaped casting, and about 4.83 h CPU-times for a 2402 s directional solidification problem of a γ(TiAl)-55 at% Al shaped casting.

CONCLUSIONS

The presently proposed and extended Direct-SIMPLE method reduces the strongly pressure-linked liquid flow problems in a dendritic alloy solidification process under an EM-field to a major computation step to solve the linear algebraic Equations (30) for the pressure change field during the time interval of Δt^{i+1}. Using this numerical algorithm, CPU-time-consuming iterative computation efforts can be avoided, especially for a 3-D solidification case with small mesh sizes. The present solidification model and the numerical solution scheme also naturally accommodate heat, mass and momentum transfer problems in a pure fluid system.

The liquid flow phenomena involved in a dendrite solidification process of alloy castings/ingots under an EM-field generally are driven simultaneously by Lorentz forces, solidification-shrinkage and the gravity, and are highly non-linear and tightly pressure-linked. The sample computations carried out for the heat and species mass transfers, and liquid flow behaviours in directionally solidifying shaped alloy castings under different types of EM-fields demonstrate the feasibility and efficient calculation performances for numerically solving a strongly coupled solidification transport problem.

NOMENCLATURE

$\mathbf{A}_{2N}$	a basic geometric unit vector for model reconstruction of any dendrite morphology
c_P	specific heat
C	concentration of a component
D	diffusion coefficient of solute
f	volume fraction
$\mathbf{F}$	force vector
$\mathbf{g}$	gravitational acceleration vector
h	latent heat of fusion
k	partition coefficient
K	permeability coefficient
P	pressure
R_f	solidification rate, $R_f = \partial f_S/\partial t$
RFVY	superficial mass flow components in y direction $(=\rho_L f_L V_y)$
RFVZ	superficial mass flow components in z direction $(=\rho_L f_L V_Z)$
t	time
T	temperature
$\mathbf{V}$	velocity vector, $\mathbf{V} = \mathbf{i}\cdot Vx + \mathbf{j}\cdot Vy + \mathbf{k}\cdot Vz$
x, y, z	3-D rectangular spatial co-ordinates

Greek letters

β	solidification shrinkage, $\beta = \rho_S/\rho_L - 1$
Δ	symbol for increment of a variable
ζ	a normalized weighting vector for growing dendrite reconstruction with the basic geometric units
θ	a non-dimensional parameter representing the sensibility of the interdendritic liquid concentration-variation in response to the SBD, $\theta = (1+\beta) - k - f_S/f_L^2$
λ	thermal conductivity
μ	dynamic viscosity
ρ	density
σ	electric conductivity
φ	a non-dimensional micro-scale parameter representing the solid back-diffusion (SBD) extent in solidifying dendrites, with a general form of $\varphi = (D_S(T)/R_f)\zeta\cdot\mathbf{A}_{2N}$
Φ	a unified micro-scale parameter accounting for any finite SBD effects in TDMAC term, $\Phi = \theta\cdot\varphi/(1+\theta\cdot\varphi)$
∇	differential operator vector, $\nabla = \mathbf{i}\cdot\partial/\partial x + \mathbf{j}\cdot\partial/\partial y + \mathbf{k}\cdot\partial/\partial z$ (in rectangular co-ordinates)

Subscripts

0	under a given condition
B	body force
G	inducted by electromagnetic field

j,k	serial numbers set specifying the position of a control volume of (j,k)
J	Joule heat
L	liquid phase or Lorentz force
Liq	liquidus
m	volume-average of mixture
S	solid phase
x, y, z	representing the x, y or z direction component of a vector

Superscripts

i	a serial number denoting a time at which various variable fields are computed
*	at solid/liquid interface or conjugate complex
$'$	temporal or revised value

ACKNOWLEDGEMENTS

The authors wish to thank the supports for the present work from a National Key Project of Grant No. 41318.4.2.9 and a Key China NNSF of Grant No. 50395102.

REFERENCES

1. Asai S. Recent development and prospect of electromagnetic processing of materials. *Science and Technology of Advanced Materials* 2000; **1**:191–200.
2. Garnier M. Electromagnetic processing of liquid materials in Europe. *ISIJ International* 1990; **30**(1):1–7.
3. Kolesnichenko AF. Electromagnetic processes in liquid material in the USSR and East European. *ISIJ International* 1990; **30**(1):8–26.
4. Evans JW. The use of electromagnetic casting for Al alloys and other metals. *Journal of Metals* May 1995; 38–41.
5. Takeuchi E. Applying MHD technology to the continuous casting of steel slab. *Journal of Metals* May 1995; 42–45.
6. Genma N, Soejima T, Saito T, Kimura M, Kaihara Y, Fukumoto H, Ayata K. The linear-motor type in-model electromagnetic stirring technique for the slab continuous caster. *ISIJ International* 1989; **29**(12):1056–1062.
7. Vives C. Effects of forced electromagnetic vibrations during the solidification of aluminum alloys: part II. Solidification in the presence of colinear variable and stationary magnetic fields. *Metallurgical and Materials Transactions B* 1996; **27B**:457–464.
8. Bennon WD, Incropera FP. A continuum model for momentum, heat and species transport in binary solid–liquid phase change system-I. Model formulation. *International Journal of Heat and Mass Transfer* 1987; **30**(10):2161–2170.
9. Xu DM, Li QC. Gravity- and solidification-shrinkage-induced liquid flow in a horizontally solidified alloy ingot. *Numerical Heat Transfer*, *Part A* 1991; **20**:203–221.
10. Xu DM. A unified micro-scale parameter approach to solidification-transport phenomena-based macrosegregation modeling for dendritic solidification: part I. Mixture average based analysis. *Metallurgical and Materials Transactions B* 2001; **32B**:1129–1141.
11. Xu DM. A unified micro-scale parameter approach to solidification-transport process-based macrosegregation modeling for dendritic solidification: part II. Numerical example computations. *Metallurgical and Materials Transactions B* 2002; **33B**:451–463.
12. Tanahashi T. Theory and application of thermo-magneto hydro dynamics (I); (II) and (III), *Tetsu-to-Hagane* 1993; **79**(2,4,5):N91–N102, N263–N281, N327–N342.
13. Xu DM, Li QC. Numerical method for solution of strongly coupled binary alloy solidification problems. *Numerical Heat Transfer*, *Part A* 1991; **20**:181–201.
14. Xu DM, Guo JJ, Fu HZ, Su YQ, Li QC. Numerical solution to T-f_S-C_L coupling in binary dendrite solidification with any solid-back diffusion effects. *Transactions of Nonferrous Metals Society of China* 2003; **13**(5): 1149–1154.

15. Bai YF, Xu DM, Guo JJ, Fu HZ. Numerical calculation for latent heat releases in alloy castings of any solidification range using an extended temperature-compensation method. *Acta Metallurgica Sinica* 2003; **39**(6):623–629.
16. Xu DM, Si GJ, An GY, Li QC. Numerical simulation of transport phenomena in solidification of multicomponent ingot using a continuum model. *Journal of Materials Science and Technology* 2001; **17**(1):67–68.
17. Patankar SV. *Numerical Heat Transfer and Fluid Flow*. Hemisphere: Washington, DC, 1980.
18. Xu DM, Wang XJ, Li QC, Pehlke RD. Control of dendrite structure and macrosegregation in directionally solidified castings with section variations. *AFS Transactions* 1997; **105**:861–868.
19. Patankar SV, Spalding DB. A calculation procedure for heat, mass and momentum transfer in three-dimensional parabolic flows. *International Journal of Heat and Mass Transfer* 1972; **15**:1787–1806.
20. Nastac L, Stefanescu DM. Macrotransport-solidification kinetics modeling of equiaxed dendritic growth: part II. Computation problems and validation on Inconel 718 superalloy castings. *Metallurgical and Materials Transactions A* 1996; **27A**:4075–4083.
21. Bai YF. *Master Thesis*, Harbin Institute of Technology, Harbin, 2002; 88–91.
22. Bai YF, Xu DM, Mao LH, Guo JJ, Fu HZ. FEM/FDM-joint simulation for transport phenomena in directional solidifying shaped TiAl casting under electromagnetic field. *ISIJ International* 2004; **44**(7):1173–1179.

